



Cite this: *Nanoscale*, 2019, **11**, 3318

## Novel tunneled phosphorus-doped WO<sub>3</sub> films achieved using ignited red phosphorus for stable and fast switching electrochromic performances†

Koo Bon-Ryul, <sup>a</sup> Kue-Ho Kim <sup>b</sup> and Hyo-Jin Ahn <sup>\*a,b</sup>

Simultaneous improvement of both the performance and stability of electrochromic devices (ECDs) to encourage their practical use in various applications, such as commercialized smart windows, electronic displays, and adjustable mirrors, by tuning the film structure and the electronic structure of transition metal oxides remains a challenging issue. In the present study, we developed novel tunneled phosphorus (P)-doped WO<sub>3</sub> films via the ignition reaction of red P. The ignited red P, which can generate exothermic energy, was used as an attractive factor to create a tunneled structure and P-doping on the WO<sub>3</sub> films. Therefore, by optimizing the effect of ignited red P on the WO<sub>3</sub> films, tunneled P-doped WO<sub>3</sub> films fabricated by using 1 wt% red P demonstrated a striking improvement of the EC performances, including both a fast switching speed (6.1 s for the colouration speed and 2.5 s for the bleaching speed) caused by the improvement of Li ion diffusion by the tunneled structure and electrical conductivity by P-doping WO<sub>3</sub> and a superb colouration efficiency (CE, 55.9 cm<sup>2</sup> C<sup>-1</sup>) as a result of increased electrochemical activity by the elaborate formation of the tunneled structure. Simultaneously, this film displayed a noticeable long-cycling stability due to a higher retention (91.5%) of transmittance modulation after 1000 electrochromic (EC) cycles as compared to bare WO<sub>3</sub> films, which can mainly be attributed to the optimizing effect of the tunneled structure to generate an efficient charge transfer and an alleviated structural variation during the insertion–extraction of Li ions. Therefore, our results suggest a valuable and well-designed strategy to manufacture stable fast-switching EC materials that are fit for various practical applications of the ECDs.

Received 31st October 2018,

Accepted 17th January 2019

DOI: 10.1039/c8nr08793h

rsc.li/nanoscale

## Introduction

Globally, in the context of serious concerns about energy depletion in the near future, technologies for energy saving or energy efficiency have been noted to be the main strategies to overcome the energy crisis. In recent years, along with electronic displays and adjustable mirrors, electrochromic devices (ECDs) have been used as a key technology for smart windows reducing heat loss and controlling incoming solar radiation to efficiently gain solar energy indoors.<sup>1–3</sup> Typically, the complementary EC devices are a combination of five functionalized layers with two different EC layers: the ion conductor layer and two transparent conducting layers.<sup>4</sup> A common assumption is

that the main factors for the improvement of EC performances (including optical modulation, colouration efficiency (CE), switching speed, and long-cycling stability) are the physical or chemical properties of EC materials to generate a balanced charge capacity and equivalent switching kinetics during electrochemical double-charge-injection.<sup>5,6</sup> As one of the most representative EC materials, tungsten oxide (WO<sub>3</sub>), corresponding to transition metal oxides with band gaps of 2.50–3.65 eV, has been extensively studied due to its advanced features of reversible colour switching from optical transparency to deep blue and for its good electrochemical stability as compared to that of organic EC materials. However, tungsten oxide (WO<sub>3</sub>) has a low CE (<30.0 cm<sup>2</sup> C<sup>-1</sup>) and a slow switching speed (>10.0 s), which remain major obstacles for its use in practical applications.<sup>7,8</sup> What is particularly important for the widespread industrial applications of the ECDs is the expansion of the operating area for large-scale devices. However, this unfortunately causes a drastic decline of the switching speed (3.0–5.0 min for 1524 × 3048 mm<sup>2</sup> of SageGlass®).<sup>9</sup> In addition, during a long-term EC cycling process related to product reliability, the ECDs exhibited a critical degradation of

<sup>a</sup>Program of Materials Science & Engineering, Convergence Institute of Biomedical Engineering and Biomaterials, Seoul National University of Science and Technology, Seoul 01811, Korea

<sup>b</sup>Department of Materials Science and Engineering, Seoul National University of Science and Technology, Seoul 01811, Korea. E-mail: hjahn@seoultech.ac.kr

†Electronic supplementary information (ESI) available. See DOI: 10.1039/c8nr08793h

transmittance modulation due to repetitive deformation of the  $\text{WO}_3$  structure by the insertion–extraction of Li ions.<sup>10,11</sup> Therefore, an effort to overcome such constraints is still needed for the development of future-oriented ECDs.

In recent years, many research strategies to enhance the EC performances, including tuning the film structure, adjusting the electronic structure, and controlling the crystalline structure, have been reported.<sup>12–14</sup> Among these, a popular research strategy is to develop porous and rough film structures with a larger specific surface area using organic materials as templates, which yields an improvement of the CE value and transmittance modulation by increasing the electrostatic contact with the electrolyte as compared to dense  $\text{WO}_3$  films.<sup>12,13</sup> Among other effective routes, one route is to adjust the electronic structure of  $\text{WO}_3$  films using Sb, Ni, and Ce elements to effectively improve the switching speeds and CE values due to a faster electrical conductivity.<sup>14,15</sup> In addition, long-cycling stability can be improved by the introduction of an opened film structure, such as mesopores and network morphologies, to accommodate the structural stress generated during the EC switching.<sup>8,16</sup> However, although many EC studies have been actively performed, to the best of our knowledge, no approach to simultaneously modify both the film structure and the electronic structure of  $\text{WO}_3$ -based films has been reported. Therefore, such an approach is a novel in terms of EC materials for the development of high-performance ECDs

with superb switching speeds, CE values, and EC cycling stability.

In the present study, we propose a novel research strategy of tunneled phosphorus (P)-doped  $\text{WO}_3$  films using the ignition reaction of red P to obtain a stable fast-switching EC performance. Red P was used as an attractive factor to generate simultaneously a tunneled surface with mesopores to accommodate the structural damage and P doping to accelerate electrical conductivity on the  $\text{WO}_3$  films. As demonstrated by our results, this approach leads to a noticeable enhancement of the switching speed and CE value, as well as ensuring a long-cycling stability of the ECDs.

## Results and discussion

The formation procedure of the tunneled P-doped  $\text{WO}_3$  films is depicted in Fig. 1a. The main driving force for forming this unique film is the ignition reaction of red P on the surface of the  $\text{WO}_3$  films. First, the  $\text{WO}_3$  films were prepared using the spin-coating of the  $\text{WCl}_6$  sol-solution on the FTO films, as described in previous reports.<sup>17,18</sup> The red P particles were introduced on the surface of the  $\text{WO}_3$  films using the spin-coating method and then heat-treated at 285 °C. During the heat treatment, burning of red P generated minimum ignition energy (MIE, 0.2 mJ) by the reaction with oxygen ( $\text{P}_4 + 5\text{O}_2 \rightarrow$

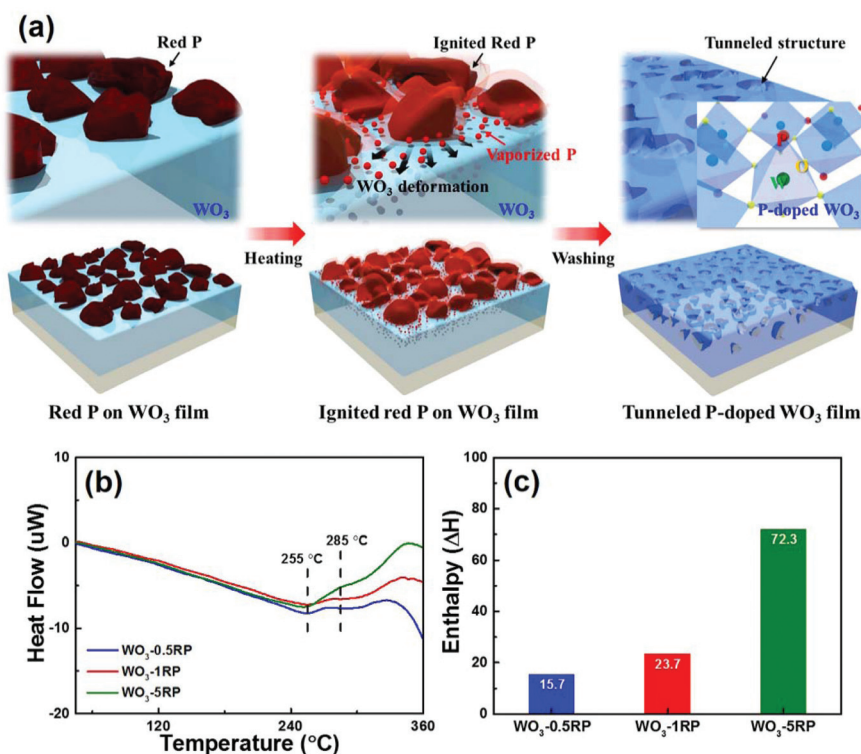


**Fig. 1** (a) Schematic diagram of the formation process for the tunneled P-doped  $\text{WO}_3$  films using ignited red P, (b) DSC curves obtained from the  $\text{WO}_3$  films with different weight percentages of red P in the temperature range of 25 to 360 °C, and (c) histograms of enthalpy values calculated using the exothermic peak of 255–285 °C.

$P_4O_{10}$ ), which was proved by an increased peak intensity of  $P_4O_{10}$  (see Fig. S1a†) and aggregation phenomena of red P particles (see Fig. S1b and c†).<sup>19,20</sup> To confirm the ignition reaction of the red P, we measured the thermal behaviour of the  $WO_3$  films with different weight percentages of the red P in the range of 35–360 °C using DSC (see Fig. 1b). All samples revealed a major exothermic peak starting from 255 °C, which, according to a previous report,<sup>21</sup> is clearly associated with the generation of the ignition reaction by the red P. In particular, with an increase of the weight percentage of the red P, there is an improvement of a major exothermic peak, which indicates the gradual acceleration of the ignition reaction by the increased red P. This result was also confirmed by the enthalpy value calculated from the endothermic peak at 255–285 °C of the DSC curve (see Fig. 1c). Therefore, this phenomenon enables a partial deformation of the  $WO_3$  near the ignited red P and vaporization of red P due to the reduced diffusion activation energy, which plays a major role in inducing the tunneled structure and P doping on the  $WO_3$  films to improve the EC performances.<sup>22,23</sup>

Fig. 2 shows the top-view FESEM images of bare  $WO_3$ ,  $WO_3$ -0.5RP,  $WO_3$ -1RP, and  $WO_3$ -5RP. In Fig. 2a, bare  $WO_3$  displays a dense and uniform structure without any discernible particulates. On the other hand, for the samples treated with the red P, the formation of the tunneled structure with the mesopores in the diameter range of 31.2–62.4 nm that can provide the relaxation sites for variation of the  $WO_3$  structure during Li ion insertion–extraction was observed over the entire surface. This result can be attributed to the optimized ignition reaction of the red P that can provide additional energy to accelerate  $WO_3$  diffusion at the surface. Therefore, at the ignition temperature of 240 °C, the film revealed a dense structure due to the nonactivated ignition reaction (see Fig. S2a†). However, when the ignition temperature increased to 340 °C, a rapid deformation of the  $WO_3$  by the excessive ignition reaction of the red P was observed, forming a distorted film structure with critical cracks to generate poor electrochemical behavior (see

Fig. S2b†).<sup>24</sup> Therefore, the optimized ignition temperature of 285 °C can realize the tunneled structure with the mesopores due to the partial deformation of the  $WO_3$  generated at the interfacial surface with the ignited red P.<sup>25,26</sup> In particular, the distribution of the tunneled structures on the films gradually increased from  $WO_3$ -0.5RP (see Fig. 2b) to  $WO_3$ -1RP (see Fig. 2c), which can be a contributing factor for improving the surface area for the electrostatic contact with the electrolyte and the efficiency of ion diffusion on the  $WO_3$ ,<sup>25</sup> as confirmed by the highest root mean square roughness ( $R_{ms}$ ) of the samples (10.5 nm for bare  $WO_3$ , 14.7 nm for  $WO_3$ -0.5RP, 20.5 nm for  $WO_3$ -1RP, and 38.5 nm for  $WO_3$ -5RP) measured from the AFM images (see Fig. S3a–d†). However, although  $WO_3$ -5RP became more dominant in the tunneled structures, it was generated due to the formation of the partial cracks on the films resulting from the excessive ignition reaction of the red P (see Fig. 2d), which can signal deterioration of the EC performances.<sup>24</sup> In addition, as can be seen in the cross-view FESEM images (see Fig. 2e–h), the structure variation that matches the top-view FESEM results was clearly observed, along with an equal film thickness in the range of 186.8–208.1 nm among the samples. Therefore, the elaborate architecture of the tunneled structure without the formation of any cracks can improve not only the switching speeds and CE values by increasing the electroactive contact with the electrolyte, but also cycling stability by effectively accommodating the charge diffusion and the expansion–contraction of the  $WO_3$  films.<sup>27</sup>

Fig. 3a shows the XRD patterns of all samples fabricated using different weight percentages of red P. The diffraction peak of bare  $WO_3$  featured a broad hump centered at around 23.1°, indicating an amorphous  $WO_3$  structure.<sup>17,28</sup> With an increase of the ignited red P, the amorphous structure was retained, whereas the peak position was gradually shifted to smaller angles. This result can be major evidence for the formation of P-doped  $WO_3$  by a partial substitution of P for O in the  $WO_3$  phase, which results from the phosphorization reaction with the  $WO_3$  by vaporized red P. This phenomenon can

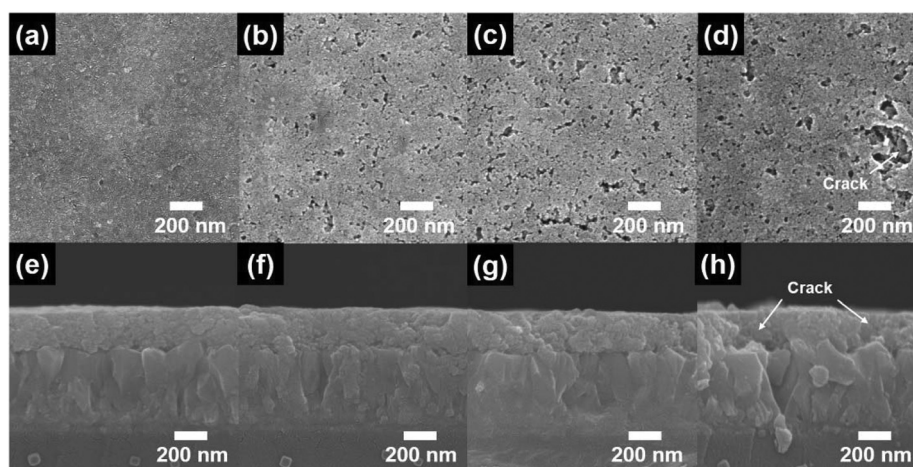


Fig. 2 (a–d) Top-view and (e–h) cross-view FESEM images of bare  $WO_3$ ,  $WO_3$ -0.5RP,  $WO_3$ -1RP, and  $WO_3$ -5RP, respectively.

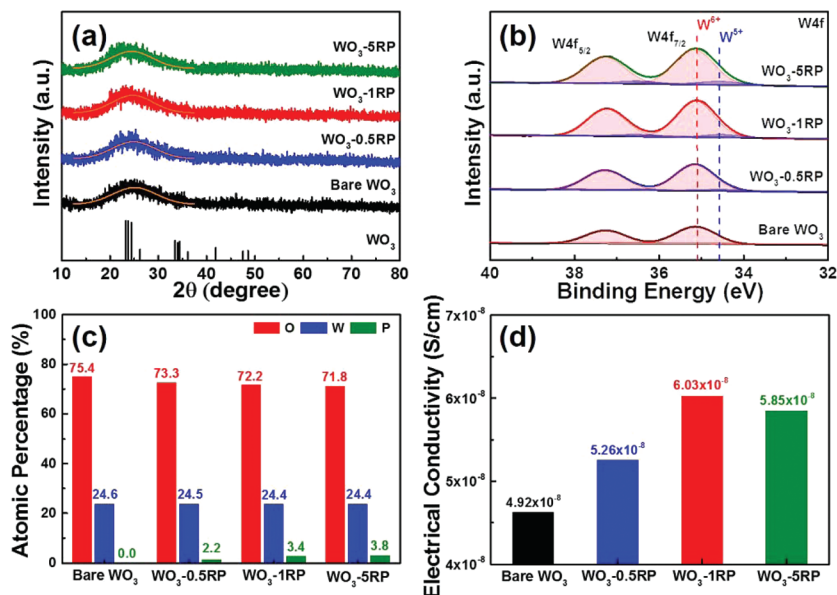


Fig. 3 (a) XRD patterns, (b) W 4f XPS core-level spectra, and histograms of (c) atomic percentages for W, O, and P elements and (d) electrical conductivity of all samples.

act as a critical factor to improve the electrical properties of the WO<sub>3</sub> films by producing oxygen vacancies due to the partial reduction of the WO<sub>3</sub> by the reaction of ignited P with O in the WO<sub>3</sub> phase, which is also confirmed by the XPS analysis and previous reports using red P by Liu *et al.* and Xu *et al.*<sup>23,29</sup> As shown in the W 4f XPS core-level spectra (see Fig. 3b), as compared to bare WO<sub>3</sub> with one pair of doublets at 35.1 eV for W 4f<sub>7/2</sub> and 37.2 eV for W 4f<sub>5/2</sub> related to the binding energy of W<sup>6+</sup>, there was an additional pair of doublets

at 34.5 eV for W 4f<sub>7/2</sub> and 36.5 eV for W 4f<sub>5/2</sub> corresponding to W<sup>5+</sup> in the samples treated with red P. This indicates the emergence of oxygen vacancies by the formed P-doped WO<sub>3</sub> phase.<sup>30</sup> In addition, the relative ratios of W<sup>5+</sup> to W<sup>6+</sup> appeared to be improved from WO<sub>3</sub>-0.5RP (0.05) to WO<sub>3</sub>-5RP (0.10), implying that the increase of ignited red P on the WO<sub>3</sub> films can enhance the number of oxygen vacancies due to the improved effect of P doping on the WO<sub>3</sub> shown in atomic percentages calculated from W, O, and P elements (see

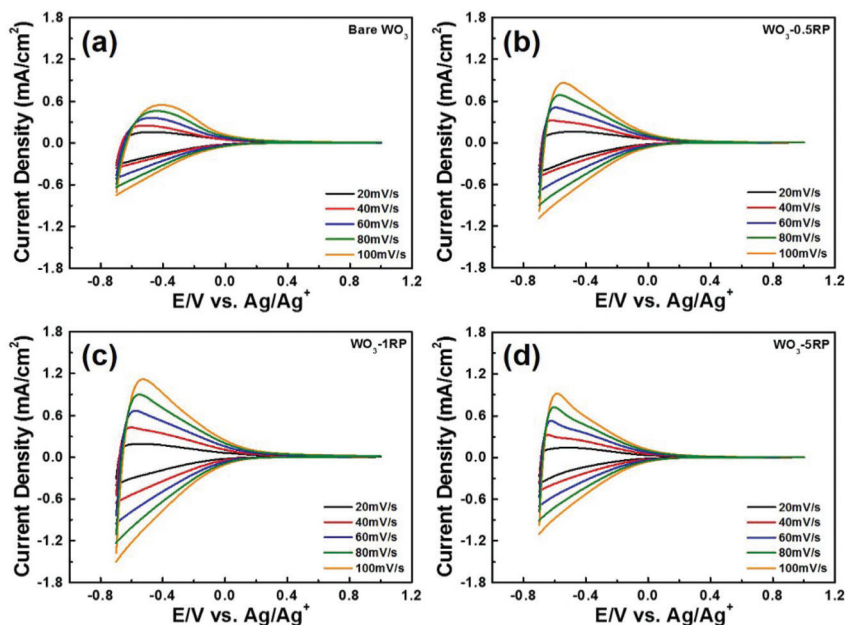


Fig. 4 (a–d) CV curves of all samples recorded between  $-0.7$  and  $1.0$  V at the varied scan rate from  $20$  to  $100$  mV s<sup>-1</sup> using the three-electrode system.

Fig. 3c), as clearly confirmed by P 2p and O 1s XPS spectra (see Fig. S4a and b,† respectively). Therefore, the accelerated effect of P doping on the WO<sub>3</sub> films *via* ignited red P can enhance electrical conductivity (see Fig. 3d) to favor the EC performance by a higher degree of electron sharing.<sup>29</sup> However, for WO<sub>3</sub>-5RP, a decreased electrical conductivity was observed, which was due to the film cracking to limit the electron transport.<sup>32</sup> The P doping on the WO<sub>3</sub> can also affect the optical bandgap. In this system, since the acceptor energy level of P was formed above the valence band of the WO<sub>3</sub>, a gradual decrease of the optical bandgap as the P-doping level increased from bare WO<sub>3</sub> to WO<sub>3</sub>-5RP was observed (see Fig. S5†).<sup>31</sup> Therefore, the ignited red P can provide WO<sub>3</sub> films with a delicate adjustment of the optoelectrical properties related to the EC performances, such as transmittance modulation, switching speeds, and CE values.<sup>32</sup>

The electrochemical behavior of the samples during the EC reaction was evaluated by the CV technique using a three-electrode system. Fig. 4 shows the CV curves traced in the potential region between -0.7 and 1.0 V (vs. Ag wire) at varied scan rates in the range of 20–100 mV s<sup>-1</sup>. During each scan, all samples showed a reversible colour variation from deep blue in the coloured state (reduction of W<sup>6+</sup> to W<sup>5+</sup>) to transparent in the bleached state (oxidation of W<sup>5+</sup> to W<sup>6+</sup>) by double insertion-extraction of electrons and Li ions in the WO<sub>3</sub>.<sup>33</sup> By comparison with the CV curve among the samples, the areas originating from the redox peaks gradually improved from bare WO<sub>3</sub> (see Fig. 4a) to WO<sub>3</sub>-1RP (see Fig. 4c) and then worsened when the ignited red P was 5 wt%, indicating that WO<sub>3</sub>-1RP had a higher electrochemical activity than the other samples due to an improved electrostatic contact by the tunneled structure without any cracks, which was able to efficiently transfer a large number of electrons and Li ions occurring in the WO<sub>3</sub> films.<sup>34</sup> Moreover, the increasing degree of peak current density with an increase of the scan rate is a way to determine the diffusion coefficient (*D*) of the Li ions for the samples, which can be calculated by using the Randles-Sevcik equation (see eqn (1)):<sup>35</sup>

$$J_p = 2.72 \times 10^5 \times D^{1/2} \times C_o \times \nu^{1/2} \quad (1)$$

where *J<sub>p</sub>*, *C<sub>o</sub>*, and *ν* are the peak current density, the concentration of active ions in the solution, and the sweep rate, respectively. As can be clearly observed in Table 1 and Fig. S6,† the Li ion diffusion coefficient increased at a higher weight percentage of red P to 1 wt%, suggesting an easy generation of the diffusion of Li ions in the films by the combined effects of

an increased distribution of the tunneled structure and an accelerated P doping in the WO<sub>3</sub> films. However, for 5 wt% red P (WO<sub>3</sub>-5RP), a decreased diffusion coefficient of Li ions was observed, despite their higher P-doping level as compared to that of WO<sub>3</sub>-1RP, implying that the film cracking complicates the Li ion diffusion in the WO<sub>3</sub> films, thereby leading to degradation of their EC kinetics.<sup>24</sup> Therefore, the optimized Li ion diffusion coefficient of WO<sub>3</sub>-1RP *via* ignited red P improved the EC performances by an efficient generation of the insertion-extraction of Li ions in the films, which was also in agreement with their electrical conductivities (see Fig. 3d).<sup>28</sup>

The trace of *in situ* optical transmittance at a wavelength of 633 nm during the EC reactions was recorded by stepping the applied potential of -0.7 V for the coloured state and 1.0 V for the bleached state for 60 s. The curve of *in situ* optical transmittance (see Fig. 5a) shows two EC performances with the transmittance modulation ( $\Delta T$ ) defined as the difference of

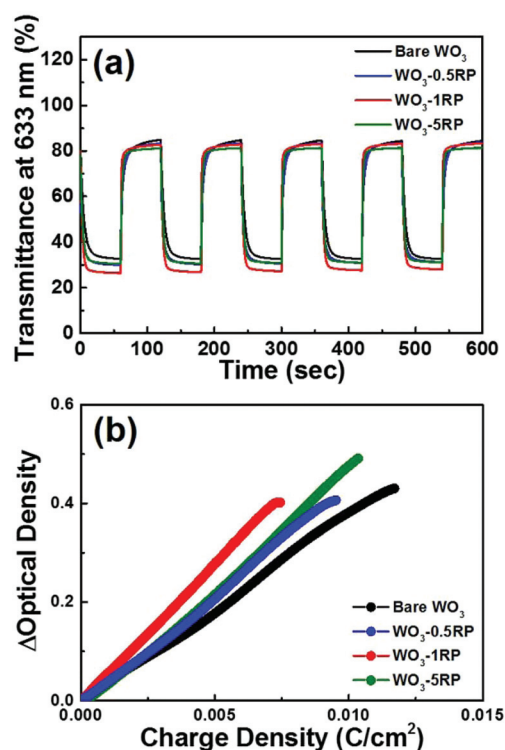


Fig. 5 (a) *In situ* optical transmittance curves of all samples traced in the stepping potential at -0.7 V for the coloured state and 1.0 V for the bleached state for 60 s and (b) optical density variation at 633 nm with respect to the inserted charge density.

Table 1 Summary of the EC performances and diffusion coefficients obtained from all samples

Samples	<i>T<sub>b</sub></i> (%)	<i>T<sub>c</sub></i> (%)	Transmittance modulation (%)	Colouration speed (s)	Bleaching speed (s)	CE (cm <sup>2</sup> C <sup>-1</sup> )	Diffusion coefficient (×10 <sup>-9</sup> cm <sup>2</sup> s <sup>-1</sup> )
Bare WO <sub>3</sub>	84.8	32.7	52.1	12.1	12.5	38.5	2.35
WO <sub>3</sub> -0.5RP	83.2	30.3	52.9	8.6	10.3	44.1	4.16
WO <sub>3</sub> -1RP	82.7	26.9	55.8	6.1	2.5	55.9	7.21
WO <sub>3</sub> -1.5RP	81.0	30.5	50.5	8.1	5.2	46.4	5.10

transmittance between the bleached state ( $T_b$ ) and the coloured state ( $T_c$ ) and the switching speed determined as the time required to reach 90% of the entire transmittance modulation at 633 nm (ref. 18 and 36) (see Table 1 for a summary). As the effect of ignited red P on the  $\text{WO}_3$  increased, due to a slight decrease of the transmittance in the bleached state from bare  $\text{WO}_3$  to  $\text{WO}_3$ -5RP resulting from the optical bandgap narrowing, the transmittance in the coloured state noticeably reduced to  $\text{WO}_3$ -1RP and then exhibited an improved value at  $\text{WO}_3$ -5RP, as a result of the variation of the electrochemical activity among the samples. This resulted in the widening of the transmittance modulation on  $\text{WO}_3$ -1RP compared to the other samples, which is also confirmed by the transmittance spectra measured in different working states (see Fig. S7†). For the switching speeds, the improved values were observed with an increase of the ignited red P from 0 to 1 wt%. This performance can mainly be attributed to an increased distribution of the tunneled structure to reduce the Li ion diffusion pathway between the  $\text{WO}_3$  material and the electrolyte and an improved electrical conductivity to efficiently transport the Li ions and electrons in the  $\text{WO}_3$  material<sup>37</sup> and is an appealing result as compared to previous reports using  $\text{WO}_3$ -based materials (see Table S1†). However, despite a high P-doping level compared to that of  $\text{WO}_3$ -1RP,  $\text{WO}_3$ -5RP showed clearly slower switching speeds, which was due to a reduction of the electrical conductivity by the film cracking. In addition, CE, which represents the variation in the optical density (OD) with inserted charge

densities ( $Q/A$ ), is another crucial factor to comprehensively evaluate the performance of EC materials. CE can be calculated from the following eqn (2) and (3):<sup>38–40</sup>

$$\text{CE} = \Delta\text{OD}/(Q/A) \quad (2)$$

$$\Delta\text{OD} = \log(T_b/T_c). \quad (3)$$

As shown in Fig. 5b, the CE values obtained by applying the potential of  $-0.7$  V to the samples were  $38.5 \text{ cm}^2 \text{ C}^{-1}$  for bare  $\text{WO}_3$ ,  $44.1 \text{ cm}^2 \text{ C}^{-1}$  for  $\text{WO}_3$ -0.5RP,  $55.9 \text{ cm}^2 \text{ C}^{-1}$  for  $\text{WO}_3$ -1RP, and  $46.4 \text{ cm}^2 \text{ C}^{-1}$  for  $\text{WO}_3$ -5RP, suggesting that  $\text{WO}_3$ -1RP had a higher performance than the other samples. This outcome can be attributed to the wide transmittance modulation by the consumption of a small charge caused from the optimized P-doped  $\text{WO}_3$  films with the tunneled structure that can provide efficient electrochemical sites and accelerated transport for inserted Li ions.

The long-cycling stability of the EC materials has been noted as an important factor related to product reliability for practical application in the devices. Therefore, we performed a continuous measurement of *in situ* optical transmittance by applying the potential between  $-0.7$  and  $1.0$  V during 1000 cycles to compare the EC cycling stability between bare  $\text{WO}_3$  and  $\text{WO}_3$ -1RP. As shown in Fig. 6a, bare  $\text{WO}_3$  revealed a decrease of the transmittance modulation after 1000 cycles (retention of 65.5%), which can be assigned to the decreased electrochemical activity by the structure distortion of  $\text{WO}_3$  (see

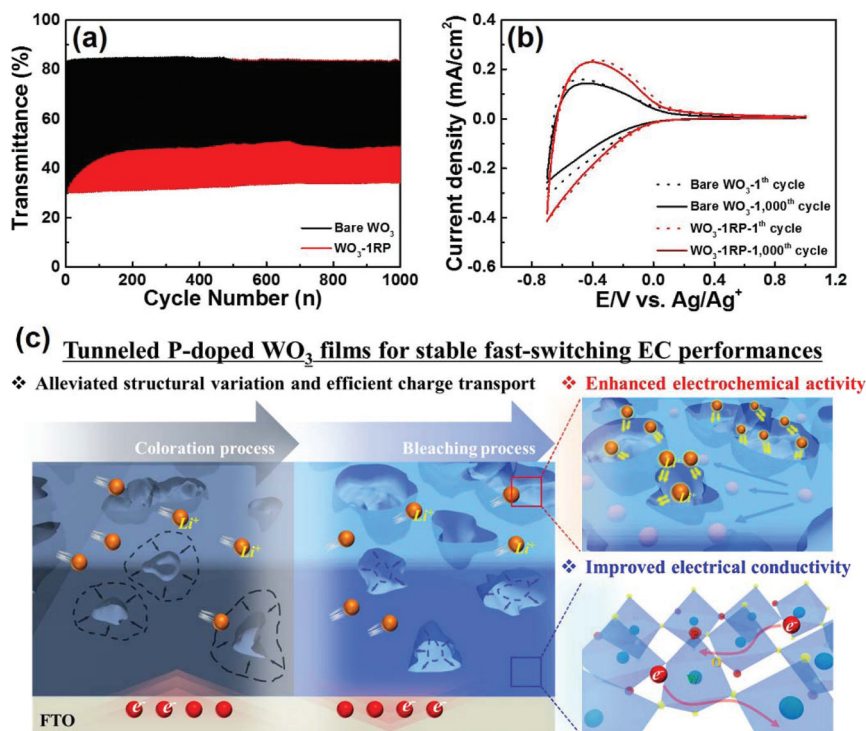


**Fig. 6** (a) Variation of *in situ* optical transmittance modulation at 633 nm for bare  $\text{WO}_3$  and  $\text{WO}_3$ -1RP during continuous CV cycling (1000 cycles) showing the EC cycling stability, (b) comparison of CV curves obtained from the 1<sup>st</sup> (dashed line) and 1000<sup>th</sup> cycle (solid line) for bare  $\text{WO}_3$  and  $\text{WO}_3$ -1RP, and (c) a possible mechanism of the improved EC performance using the tunneled P-doped  $\text{WO}_3$  films.

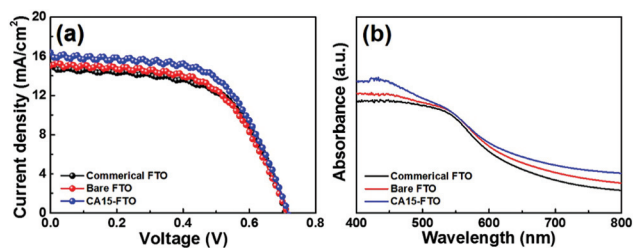


Fig. 7 (a) Photocurrent–voltage ( $J$ – $V$ ) curves measured from the DSSCs using the commercial FTO, bare FTO, and CA15-FTO as a TCO of the working electrode and (b) absorption spectra of the half cells with the FTO films and  $\text{TiO}_2$  with the dye.

also Fig. 6b).<sup>10,41,42</sup> Interestingly, we also observed that  $\text{WO}_3$ -1RP maintained a wide transmittance modulation with a retention of 91.5% as compared to the initial value after 1000 cycles. This increase (26.0%) of the cycling stability was mainly induced by the tunneled structure to facilitate the charge transfer in the  $\text{WO}_3$  films and an alleviated expansion of the  $\text{WO}_3$  structure during the EC cycling, thus leading to a stable electrochemical activity after 1000 cycles (see Fig. 6b). Overall, the tunneled P-doped  $\text{WO}_3$  films achieved a surprising EC performance with fast switching speeds, high EC values, and stable long-cycling stability, all of which can be attributed to the effective functionalities of the tunneled structure and P-doping on the  $\text{WO}_3$  films caused by the ignition reaction of red P (see Fig. 6c). Firstly, fast switching speeds (6.1 s for the colouration speed and 2.5 s for the bleaching speed) were induced by a reduced diffusion pathway of Li ions by the mesopores of the tunneled structure and an improved electrical conductivity by the oxygen vacancies of P-doped  $\text{WO}_3$ . The improvement of the CE value ( $55.9 \text{ cm}^2 \text{ C}^{-1}$ ) was due to an enhanced electrochemical activity as a result of improved electrostatic contact by the tunneled structure without any cracks. In addition, an outstanding long-cycling stability (91.5%) was caused by a unique tunneled structure which enables an efficient charge transfer and relaxation of  $\text{WO}_3$  variation during the insertion and extraction of Li ions (Fig. 7).

## Conclusions

In the present study, we successfully fabricated novel tunneled P-doped films using the ignition reaction of red P. By optimizing the ignited red P, this enabled not only the elaborate formation of a tunneled structure with mesopores by a partial deformation of the  $\text{WO}_3$ , but also P doping (3.4 at%) into the  $\text{WO}_3$  by substitution of vaporized P for O sites of the  $\text{WO}_3$  phase. Therefore, the tunneled P-doped films ( $\text{WO}_3$ -1RP) exhibited a striking improvement of the EC performances with both fast switching speeds (6.1 s for the colouration speed and 2.5 s for the bleaching speed) and a superb CE value ( $55.9 \text{ cm}^2 \text{ C}^{-1}$ ), all of which were mainly related to the attractive functionalities. Specifically, switching speeds were improved due to the synergistic effects to accelerate the Li ion diffusion by the tun-

neled structure with the mesopores and the electrical conductivity by P-doped  $\text{WO}_3$  with increased oxygen vacancies. In addition, the increased CE value resulted from an efficient electroactive contact with the electrolyte by the tunneled structure offering  $\text{WO}_3$  materials an increased electrochemical activity, causing the widening of the transmittance modulation as a small charge was inserted. More interestingly, this film was found to have a highly stable long-cycling retention (91.5%) after 1000 cycles, which can be attributed to the efficient charge transfer and relaxed expansion–contraction of the tunneled structure during the Li-ion insertion–extraction. Therefore, our results offer a unique approach to modify both the film structure and the doping structure of the  $\text{WO}_3$ -based films for the improvement of the EC performances and provide meaningful insights for further research on the extensions of the practical application of the ECDs.

## Experimental section

Tunneled P-doped  $\text{WO}_3$  films were developed by the ignition reaction of red P. To prepare the  $\text{WO}_3$  films, 10 wt% tungsten(vi) chloride ( $\text{WCl}_6$ , Aldrich) was added in 2-propanol ( $(\text{CH}_3)_2\text{CHOH}$ , Aldrich). After stirring, the  $\text{WCl}_6$  sol-solution was spin-coated onto a commercial FTO glass (Pilkington,  $8.0 \Omega \square^{-1}$ ) at a rotation speed of 2000 rpm for 30 s. The resultant films were then annealed at 300 °C in air for 1 h to form the  $\text{WO}_3$  films (thereafter referred to as bare  $\text{WO}_3$ ). The red P solutions were prepared by mixing red P ((Hill Notation) P, Aldrich) and 2-propanol for 1 h and then introduced onto the as-prepared  $\text{WO}_3$  films using the spin-coating method at 2000 rpm for 30 s, in which the weight percentage of red P to 2-propanol was adjusted to 0.5, 1, and 5 wt% for optimizing their EC performances. The samples were then heat-treated at 285 °C to induce the ignition reaction of red P on the  $\text{WO}_3$  films, which resulted in the formation of tunneled P-doped  $\text{WO}_3$  films. The obtained films using 0.5, 1, and 5 wt% red P were labelled  $\text{WO}_3$ -0.5RP,  $\text{WO}_3$ -1RP, and  $\text{WO}_3$ -5RP, respectively.

The thermal characterization was further investigated using differential scanning calorimetry (DSC, DSC-60, Shimadzu). The morphologies were revealed by field-emission scanning electron microscopy (FESEM, Hitachi S-4800) and atomic force microscopy (AFM, diDimensionTM 3100). The crystalline structure and chemical composition were measured using X-ray diffraction (XRD, Rigaku D/Max-2500 diffractometer using  $\text{Cu K}_\alpha$  radiation) and X-ray photoelectron spectroscopy (XPS, AXIS ultra-delay line detector equipped with an Al  $\text{K}_\alpha$  X-ray source, KBSI Daedeok Headquarters), respectively. The electrical and optical properties were determined using a Hall-effect measurement system (Ecopia, HMS-3000) and ultraviolet-visible (UV-vis) spectroscopy (Perkin-Elmer, Lambda-35), respectively. The electrochemical properties were determined using a potentiostat/galvanostat (PGSTAT302N, FRA32 M, Metrohm Autolab B.V., the Netherlands) in a three-electrode cell configuration with Pt wire as the counter electrode, Ag wire as the reference electrode, and 1 M  $\text{LiClO}_4$  in propylene

carbonate (PC) as the electrolyte. The EC performances were *in situ* characterized using ultraviolet-visible (UV-vis) spectroscopy (Perkin-Elmer, Lambda-35) together with a potentiostat/galvanostat.

## Conflicts of interest

There are no conflicts of interest to declare.

## Acknowledgements

This study was supported by the Advanced Research Project funded by the SeoulTech (Seoul National University of Science and Technology).

## Notes and references

- H. Park, D. S. Kim, S. Y. Hong, C. Kim, J. Y. Yun, S. Y. Oh, S. W. Jin, Y. R. Jeong, G. T. Kim and J. S. Ha, *Nanoscale*, 2017, **9**, 7631.
- G. J. Stec, A. Lauchner, Y. Cui, P. Nordlander and N. J. Halas, *ACS Nano*, 2017, **11**, 3254.
- K. Bange and T. Gambke, *Adv. Mater.*, 1990, **2**, 10.
- W. Dong, Y. Lv, L. Xiao, N. Zhang and X. Liu, *ACS Appl. Mater. Interfaces*, 2016, **8**, 33842.
- K. R. Reyes-Gil, Z. D. Stephens, V. Stavila and D. B. Robinson, *ACS Appl. Mater. Interfaces*, 2015, **7**, 2202.
- L. Zhu, C. K. N. Peh, T. Zhu, Y.-F. Lim and G. W. Ho, *J. Mater. Chem. A*, 2017, **5**, 8343.
- G. Cai, P. Darmawan, M. Cui, J. Chen, X. Wang, A. L.-S. Eh, S. Magdassi and P. S. Lee, *Nanoscale*, 2016, **8**, 348.
- J. Zhang, X. L. Wang, X. H. Xia, C. D. Gu and J. P. Tu, *Sol. Energy Mater. Sol. Cells*, 2011, **95**, 2107.
- M. Casini, *Int. J. Civ. Struct. Eng.*, 2016, **2**, 230.
- D. Ma, J. Wang, H. Wei and Z. Guo, *Multifunctional nanocomposites for energy and environmental applications*, Wiley-VCH, Weinheim, 2018.
- D. Zhou, B. Che, J. Kong and X. Lu, *J. Mater. Chem. C*, 2016, **4**, 8041.
- H. Zhang, G. Duan, G. Liu, Y. Li, X. Xu, Z. Dai, J. Wang and W. Cai, *Nanoscale*, 2013, **5**, 2460.
- T. Brezesinski, D. F. Rohlffing, S. Sallard, M. Antonietti and B. M. Smarsly, *Small*, 2006, **2**, 1203.
- R. Mukherjee and P. P. Sahay, *J. Alloys Compd.*, 2016, **660**, 336.
- T. Kunyapat, F. Xu, N. Neate, N. Wang, A. D. Sanctis, S. Russo, S. Zhang, Y. Xia and Y. Zhu, *Nanoscale*, 2018, **10**, 4718.
- W.-Q. Wang, X.-L. Wang, X.-H. Xia, Z.-J. Yao, Y. Zhong and J.-P. Tu, *Nanoscale*, 2018, **10**, 8162.
- B.-R. Koo, K.-H. Kim and H.-J. Ahn, *Appl. Surf. Sci.*, 2018, **453**, 238.
- B.-R. Koo and H.-J. Ahn, *Nanoscale*, 2017, **9**, 17788.
- H. Haase, *Electrostatic hazards: their evaluation and control*, Wiley-VCH, Weinheim, 1978.
- M. Edmund, P. Passmore and L. D. George, *J. Illum. Eng. Soc.*, 1978, **7**, 202.
- S. M. Mostashari, *Cellul. Chem. Technol.*, 2009, **43**, 199.
- D.-Y. Sin, I.-K. Park and H.-J. Ahn, *RSC Adv.*, 2016, **6**, 58823.
- Y. Liu, A. Zhang, C. Shen, Q. Liu, X. Cao, Y. Ma, L. Chen, C. Lau, T.-C. Chen, F. Wei and C. Zhou, *ACS Nano*, 2017, **11**, 5530.
- M. Deepa, T. K. Saxena, D. P. Singh, K. N. Sood and S. A. Agnihotry, *Electrochim. Acta*, 2006, **51**, 1974.
- C. J. Brinker, A. J. Hurd, P. R. Schunk, G. C. Frye and C. S. Ashley, *J. Non-Cryst. Solids*, 1992, **147**, 424.
- Q. Zhang, T. P. Chou, B. Russo, S. A. Jenekhe and G. Cao, *Angew. Chem., Int. Ed.*, 2008, **120**, 2436.
- G. Cai, M. Cui, V. Kumar, P. Darmawan, J. Wang, X. Wang, A. L.-S. Eh and P. S. Lee, *Chem. Sci.*, 2016, **7**, 1373.
- J. Han, K.-W. Ko, S. Sarwar, M.-S. Lee, S. Park, S. Hong and C.-H. Han, *Electrochim. Acta*, 2018, **278**, 396.
- J. Xu, Z. Liao, J. Zhang, B. Gao, P. K. Chu and K. Huo, *J. Mater. Chem. A*, 2018, **6**, 6916.
- B.-R. Koo, J.-W. Bae and H.-J. Ahn, *Ceram. Int.*, 2017, **43**, 6124.
- D.-K. Hwang, H.-S. Kim, J.-H. Lim, J.-Y. Oh, J.-H. Yang and S.-J. Park, *Appl. Phys. Lett.*, 2005, **86**, 151917.
- M. A. Arvizu, G. A. Niklasson and C. G. Granqvist, *Chem. Mater.*, 2017, **29**, 2246.
- L. Xiao, Y. Lv, W. Dong, N. Zhang and X. Liu, *ACS Appl. Mater. Interfaces*, 2016, **8**, 27107.
- G. Yuan, C. Hua, S. Khan, S. Jiang, Z. Wu, Y. Liu, J. Wang, C. Song and G. Han, *Electrochim. Acta*, 2018, **260**, 274.
- H. Kim, D. Choi, K. Kim, W. Chu, D.-M. Chun and C. S. Lee, *Sol. Energy Mater. Sol. Cells*, 2018, **177**, 44.
- Z. Bi, X. Li, Y. Chen, X. He, X. Xu and X. Gao, *ACS Appl. Mater. Interfaces*, 2017, **9**, 29872.
- Y. Li, W. A. McMaster, H. Wei, D. Chen and R. A. Caruso, *ACS Appl. Nano Mater.*, 2018, **1**, 2552.
- A. Zhou, X. Liu, Y. Dou, S. Guan, J. Han and M. Wei, *J. Mater. Chem. C*, 2016, **4**, 8284.
- G. Cai, M. Cui, V. Kumar, P. Darmawan, J. Wang, X. Wang, A. L.-S. Eh, K. Qian and P. S. Lee, *Chem. Sci.*, 2016, **7**, 1373.
- D. Zhou, D. Xie, X. Xia, X. Wang, C. Gu and J. Tu, *Sci. China: Chem.*, 2017, **60**, 3.
- J. Zhou, Y. Wei, G. Luo, J. Zheng and C. Xu, *J. Mater. Chem. C*, 2016, **4**, 1613.
- G.-F. Cai, J.-P. Tu, D. Zhou, L. Li, J.-H. Zhang, X.-L. Wang and C.-D. Gu, *CrystEngComm*, 2014, **16**, 6866.